

# Effective node adaption for grid-free semi-Lagrangian advection

JÖRN BEHRENS, ARMIN ISKE and STEFAN PÖHN

**Abstract.** Grid-free adaptive semi-Lagrangian advection, as recently suggested in [3], relies on two basic ingredients: scattered data approximation and a customized strategy for the adaption (coarsening and refinement) of the scattered nodes. In this paper, effective rules for the node adaption are proposed. The practicability of the grid-free advection method is illustrated in our numerical examples by simulation of tracer transportation in the arctic stratosphere.

*Keywords:* Adaptive advection schemes, semi-Lagrangian method, grid-free methods, radial basis functions, tracer transport simulation.

## 1 Introduction

In a previous paper [3], a new *grid-free* adaptive advection scheme has been proposed for the purpose of numerically solving the linear advection equation

$$\frac{\partial c}{\partial t} + \frac{dx}{dt} \cdot \nabla c = 0$$

in  $\bar{\Omega} = I \times \Omega$ , where  $I = [0, T] \subset \mathbb{R}$ ,  $T > 0$ , is a compact time interval, and where  $c : \bar{\Omega} \rightarrow \mathbb{R}$  models the time-dependent distribution of the *concentration* in the computational domain  $\Omega = \mathbb{R}^d$ ,  $d \geq 1$ .

The method in [3] is a combination of an adaptive semi-Lagrangian method (SLM) and the grid-free radial basis function (RBF) interpolation. In contrast to the similar but *grid-based* SLM advection scheme [1, 2], the adaption in the grid-free approach [3] does merely rely on the insertion (refinement) and removal (coarsening) of nodes rather than on local modifications of a finite element mesh. In order to decide where to insert or remove single nodes, an a posteriori error indicator is used.

With the absence of any connectivities between the nodes, a grid-free adaption scheme is in general more flexible than a grid-based one, where e.g. special treatment of hanging nodes is required for maintaining a valid mesh, cf. [1]. Moreover, grid-based methods are prohibitively expensive in higher dimensions, giving grid-free methods, often also referred to as *mesh-less methods*, an other advantage. But grid-free adaptive advection requires effective and customized rules for the refinement and coarsening of the nodes.

Indeed, the selected node adaption strategy does significantly contribute to the method's performance in terms of its computational costs and approximation behaviour: At any time step, the current node distribution affects the quality of (a) the interpolation at upstream points; (b) the a posteriori error indication; (c) the evaluation of the model.

The node adaption in [3] uses effective rules that are well-motivated by available error estimates for RBF interpolation. But this important aspect has widely been omitted in [3]. In this paper, we focus on explaining the details of the node adaption, being subject of Section 4, including a discussion on the a posteriori error indication. For further details concerning the implementation of the scheme, we refer to the recent work [11].

In order to make this paper self-contained, we first briefly explain the grid-free adaptive SLM in the following Section 2. The relevant features of RBF interpolation are then discussed in Section 3 with special emphasis on local error estimates. For a more comprehensive overview over RBF, we refer the reader to the survey papers [5, 7, 12, 14]. The SLM is explained in the textbook [10], its convergence behaviour is subject of the discussion in [8], and its application in meteorology is reviewed in [15].

A realistic test case scenario in Section 5 concerning the advection of a tracer in the arctic stratosphere confirms the applicability of the grid-free method, and it shows the effectiveness of the proposed adaption rules.

## 2 Adaptive Semi-Lagrangian Advection

The adaptive advection scheme in [3] is based on a semi-Lagrangian time discretization. For each node  $\xi$  in the current node set  $\Xi \equiv \Xi^t$  (at time  $t$ ), an approximation  $x$  to its corresponding *upstream point* is computed, before the concentration value  $c(t, x)$  is approximated by using RBF interpolation at a specific set  $\mathcal{N} \subset \Xi$  of *neighbouring nodes* of  $x$ . The advection is then accomplished by letting  $c(t + \Delta t, \xi) = c(t, x)$ .

Having computed all values  $c(t + \Delta t, \xi)$ ,  $\xi \in \Xi$ , the node set  $\Xi$  is modified by the removal (coarsening), and the insertion (refinement) of nodes, yielding a new node set  $\Xi \equiv \Xi^{t+\Delta t}$  (at time  $t + \Delta t$ ). The adaption of the nodes, i.e. the refinement and coarsening, relies on a specific a posteriori error indicator to be explained in Section 4. Be it sufficient for the moment to say that the error indicator assigns to each node  $\xi \in \Xi$  a value  $\eta(\xi)$  reflecting the local approximation quality of RBF interpolation around  $\xi$ . The values  $\eta(\xi)$ ,  $\xi \in \Xi$ , are then used as criteria for the removal and insertion of nodes. A flowchart of the entire algorithm is shown in Figure 1.

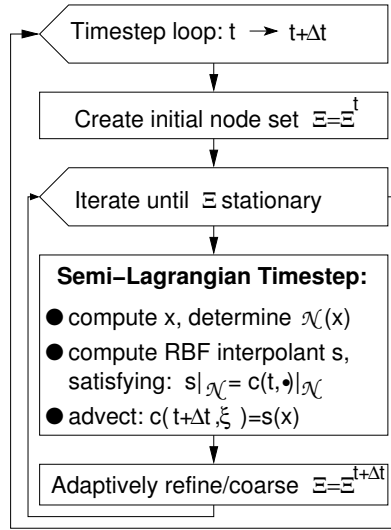


Figure 1: Flowchart of the grid-free adaptive semi-Lagrangian method.

### 3 Radial Basis Function Interpolation

In this section, we explain the relevant features of the RBF interpolation scheme. In particular, the design of the adaption rules is motivated here. To this end, for any  $x \in \Omega$  let  $\mathcal{N} \equiv \mathcal{N}(x) \subset \Xi$  be a set of neighbouring nodes of  $x$ . Since  $t \in I$  is fixed during the interpolation, we let  $c \equiv c(t, \cdot)$  for the sake of notational simplicity. Suppose we wish to approximate the value  $c(x)$  from given *current* concentration values  $c(\nu)$ ,  $\nu \in \mathcal{N}$ , by solving the interpolation problem

$$s(\nu) = c(\nu), \quad \text{for all } \nu \in \mathcal{N}. \quad (1)$$

According to the RBF interpolation scheme, for a fixed radial function  $\phi : [0, \infty) \rightarrow \mathbb{R}$  the interpolant  $s$  in (1) has the form

$$s = \sum_{\nu \in \mathcal{N}} \lambda_{\nu} \phi(\|\cdot - \nu\|) + \sum_{\ell=1}^Q \mu_{\ell} p_{\ell}, \quad (2)$$

where  $\|\cdot\|$  is the Euclidean norm on  $\mathbb{R}^d$ . Moreover, the functions  $p_1, \dots, p_Q$  are a basis of the linear space  $\Pi_m^d$  containing all real-valued  $d$ -variate polynomials of order at most  $m$ , i.e.  $Q = \binom{m-1+d}{d}$ . The order  $m$  of the polynomial part of  $s$  depends on the particular choice of  $\phi$ . Table 3 gives a list of commonly used radial basis functions along with their corresponding order  $m$ . A more comprehensive listing can be found in [14].

Hence, when using Thin Plate Splines, the polynomial part in (2) is linear, for Multiquadrics it is constant, and for Gaussians and Inverse Multiquadrics

Name	$\phi(r)$	$m$	$F_\phi^2(h)$
Gaussians	$\phi(r) = e^{-r^2}$	0	$e^{-\delta/h^2}, \delta > 0$
Thin Plate Splines	$\phi(r) = r^2 \log(r)$	2	$h^2$
Multiquadrics	$\phi(r) = (r^2 + 1)^{1/2}$	1	$e^{-\delta/h}, \delta > 0$
Inverse Multiquadrics	$\phi(r) = (r^2 + 1)^{-1/2}$	0	$e^{-\delta/h}, \delta > 0$

Table 1: Radial basis functions.

there is no polynomial to be added in (2). Regarding the above interpolation problem (1) we obtain  $N = \#\mathcal{N}$  linear equations in  $N+Q$  unknown variables  $\lambda_\nu$ ,  $\nu \in \mathcal{N}$ , and  $\mu_\ell$ ,  $1 \leq \ell \leq Q$ . The additional degrees of freedom are eliminated by adding the  $Q$  side conditions

$$\sum_{\nu \in \mathcal{N}} \lambda_\nu p(\nu) = 0, \quad \text{for all } p \in \Pi_m^d,$$

which naturally arise from the properties of  $\phi$  and the chosen ansatz (2), cf. [7] for more details.

Now let us turn to local error estimates on  $|c(x) - s(x)|$  at  $x \in \Omega$ . For the abovementioned radial basis functions in Table 3 these estimates are of the form

$$|c(x) - s(x)| \leq C \cdot P_{\phi, \mathcal{N}}(x) \quad (3)$$

where the constant  $C$  solely depends on the function  $c$ , and the *power function*  $P_{\phi, \mathcal{N}}(x)$ , being the norm of the error functional at  $x$ , depends only on  $\phi$  and  $\mathcal{N}$ . The power function can further be bounded above by an estimate of the form

$$P_{\phi, \mathcal{N}}(x) \leq F_\phi(h_{\mathcal{N}, \varrho}(x)),$$

which leads in combination with (3) to

$$|c(x) - s(x)| \leq C \cdot F_\phi(h_{\mathcal{N}, \varrho}(x)). \quad (4)$$

Here,  $F_\phi : [0, \infty) \rightarrow [0, \infty)$  is a monotonic function, with  $F_\phi(0) = 0$ , which depends only on  $\phi$ . Table 3 shows the form of  $F_\phi$  for the list of choices for  $\phi$ . As to the argument of  $F_\phi$  in (4),

$$h_{\mathcal{N}, \varrho}(x) = \sup_{\|y-x\| < \varrho} d_{\mathcal{N}}(y)$$

is the local *fill distance* of  $\mathcal{N}$  around  $x$ , with

$$d_{\mathcal{N}}(y) = \min_{\nu \in \mathcal{N}} \|y - \nu\|$$

being the Euclidean distance between the point  $y$  and the set  $\mathcal{N}$ . The radius  $\varrho$  in (4) does depend on both the basis function  $\phi$  and the point set  $\mathcal{N}$  [14].

## 4 Adaption Rules

### 4.1 Error Indication

An effective strategy for the adaptive modification of the nodes requires well-motivated refinement and coarsening rules as well as a customized error indicator. We understand the error indicator  $\eta : \Xi \rightarrow [0, \infty)$  as a function of the current node set  $\Xi$  which serves to assign a *significance* value  $\eta(\xi)$  to each  $\xi \in \Xi$ . The value  $\eta(\xi)$  is required to reflect the local approximation quality of the interpolation around  $\xi \in \Xi$ . The significances  $\eta(\xi)$ ,  $\xi \in \Xi$ , are then used in order to flag single nodes  $\xi \in \Xi$  as “to be refined” or “to be coarsened” according to the following criteria.

**Definition 1** *Let  $\eta^* = \max_{\xi \in \Xi} \eta(\xi)$ , and let  $\theta_{\text{crs}}, \theta_{\text{ref}}$  be two tolerance values satisfying  $0 < \theta_{\text{crs}} < \theta_{\text{ref}} < 1$ . We say that a node  $\xi \in \Xi$  is **to be refined**, if  $\eta(\xi) > \theta_{\text{ref}} \cdot \eta^*$ , and  $\xi$  is **to be coarsened**, if  $\eta(\xi) < \theta_{\text{crs}} \cdot \eta^*$ .*

In our numerical examples typical choices for the relative tolerance values are  $\theta_{\text{crs}} = 0.1$  and  $\theta_{\text{ref}} = 0.2$ . Note that a node  $\xi$  cannot be refined and be coarsened at the same time; in fact, it may neither be refined nor be coarsened.

Now let us turn to the definition of the error indicator  $\eta$ . We follow along the lines of [9], where a local scheme for the detection of discontinuities of a surface from scattered data was developed, and we let

$$\eta(\xi) = |c(\xi) - s(\xi)|,$$

where the RBF interpolant  $s \equiv s_{\mathcal{N}}$  matches current concentration values of  $c$  at a neighbouring set  $\mathcal{N} \equiv \mathcal{N}(\xi) \subset \Xi \setminus \{\xi\}$  of nodes, so that (1) holds. In our numerical examples, we preferred to use Thin Plate Splines, whose corresponding interpolation scheme achieves to reconstruct linear polynomials. In this case, the value  $\eta(\xi)$  vanishes whenever the local concentration  $c$  around  $\xi$  is a linear function. Moreover, the value  $\eta(\xi)$  is small whenever the reproduction of  $c$  by  $s$  around  $\xi$  is good. In contrast, a high value of  $\eta(\xi)$  typically indicates that the concentration  $c$  around  $\xi$  is subject to strong variation.

## 4.2 Coarsening and Refinement

In order to balance the approximation quality of the model against the required computational complexity we insert new nodes into regions where the value of  $\eta$  is high (refinement), whereas we remove nodes from  $\Xi$  in regions where the value of  $\eta$  is small (coarsening).

To avoid additional computational overhead and complicated data structures, effective adaption rules are required to be as simple as possible. In particular, these rules ought to be given by *local* operations on the current node set  $\Xi$ . The following coarsening rule is in fact very easy and, in combination with the refinement, it turned out to be very effective as well.

**Definition 2** *A node  $\xi \in \Xi$  is coarsened by its removal from the current node set  $\Xi$ , i.e.  $\Xi$  is modified by letting  $\Xi = \Xi \setminus \{\xi\}$ .*

As concerns the refinement of a node  $\xi \in \Xi$ , the starting point for the design of a customized refinement rule is the estimate (4). The upper bound on the local error around  $\xi$  motivates us to build the refinement merely on the local distribution of the nodes around  $\xi$ , rather than on any complicated and costly evaluation scheme involving  $\phi$ .

Regarding the right hand side of (4), we wish to insert a few new nodes in a neighbourhood  $U \equiv U(\xi) \subset \Omega$  of  $\xi$  such that  $h_{\varrho, \mathcal{N}}$  is as much as possible reduced in  $U$ . This is done by reducing the distance function  $d_{\mathcal{N}}$  in  $U$ . But this requires some notational preparation.

Recall that for a fixed node set  $\Xi \subset \mathbb{R}^d$  and any  $\xi \in \Xi$ , the *Voronoi tile*

$$V_{\Xi}(\xi) = \{x \in \mathbb{R}^d : d_{\Xi}(x) = \|x - \xi\|\} \subset \mathbb{R}^d$$

of  $\xi$  w.r.t.  $\Xi$  contains all points in  $\mathbb{R}^d$  whose nearest point in  $\Xi$  is  $\xi$ . The tile  $V_{\Xi}(\xi)$  is a convex polytope whose vertices are referred to as the *Voronoi points*, forming a finite point set  $\mathcal{V}_{\xi}$  in the neighbourhood of  $\xi$ . Figure 4.2 shows the Voronoi tile  $V_{\Xi}(\xi)$  of a point  $\xi$  along with the set  $\mathcal{V}_{\xi}$  of its Voronoi points. For more details on Voronoi diagrams, we refer to [13].

Now observe that for  $\xi \in \mathcal{N}$  the distance function  $d_{\mathcal{N}}$  is convex on  $V_{\Xi}(\xi)$ . Moreover, it has local maxima at the Voronoi points in  $\mathcal{V}_{\xi}$ . As confirmed by numerical experiments, for any  $\phi$  in Table 3, the power function  $P_{\phi, \mathcal{N}}$  does also attain its local maxima at Voronoi points. Altogether, this gives rise to define the local refinement of nodes on the basis of these observations.

**Definition 3** *A node  $\xi \in \Xi$  is refined by the insertion of its Voronoi points into the current node set  $\Xi$ , i.e.  $\Xi$  is modified by letting  $\Xi = \Xi \cup \mathcal{V}_{\xi}$ .*

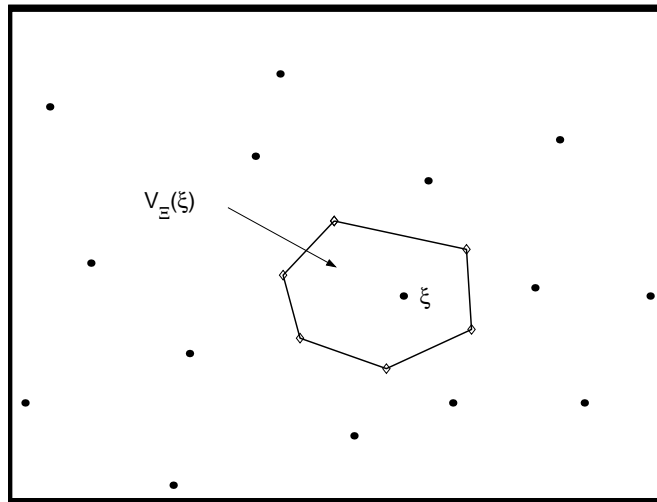


Figure 2: Refinement of the node  $\xi$ . The Voronoi points ( $\diamond$ ) are inserted.

## 5 Tracer Advection over the Arctic

The proposed grid-free advection method has been applied to a tracer transport problem in the arctic stratosphere. When investigating ozone depletion over the arctic, one interesting question is whether air masses with low ozone concentration are advected into southern regions. Our experiments are still purely academic since no realistic initial tracer concentration is assumed and no chemical reaction is included in the model. However, with our simplified advection model, taking realistic wind fields, filamentation of the tracer cloud can be observed which corresponds to airborne observations [4].

Wind data were taken from the high-resolution regional climate model (HIRHAM) [6]. HIRHAM resolves the arctic region with a horizontal resolution of  $0.5^\circ$ . It is forced at the lateral and lower boundaries by ECMWF reanalysis data. We consider the transport of a passive tracer at 73.4 hPa in the vortex. This corresponds to an altitude of 18 km. The wind field reproduces the situation in January 1990. Because stratospheric motion is thought to be constrained largely within horizontal layers, we use a two-dimensional horizontal transport scheme here. Wind data represent the  $(u, v)$ -values in the mentioned layer of the three-dimensional HIRHAM model. The wind field and the initial tracer distribution for the advection experiment are shown in Figure 3.

A comparison of the results from a grid-free simulation with a grid-based version is shown in Figure 4. Note that the grid-free simulation achieves to capture the features of the tracer well with a very accurate reproduction of

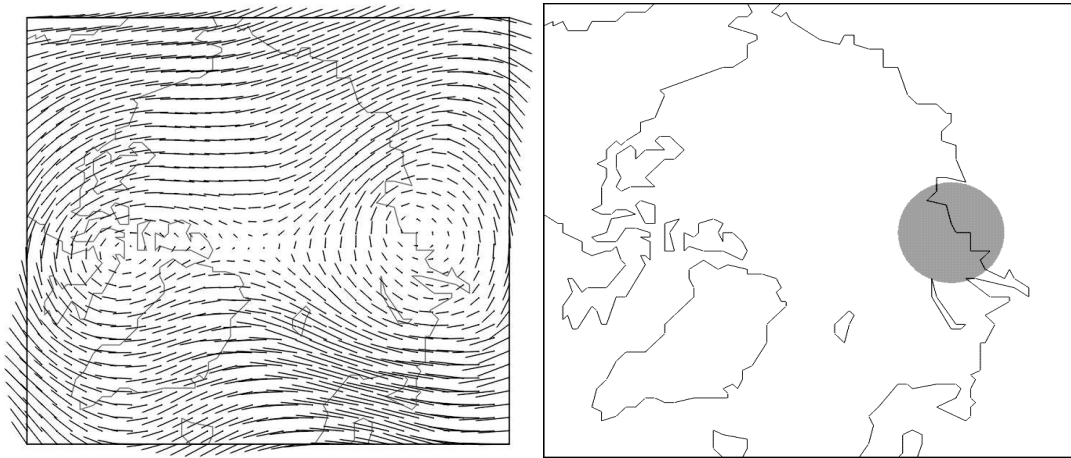


Figure 3: Wind field and initial situation for tracer advection. The artificial tracer cloud is positioned in the center of the polar vortex. Continental outlines are given for orientation (Greenland in the lower left part).

the filamentation. The corresponding node distribution is shown in Figure 5. Note that the adaptive refinement and coarsening of the nodes essentially leads to a heterogeneous node distribution. This serves to model the finer details of the tracer effectively at reasonable computational costs.

## Acknowledgments

The second author was partly supported by the European Union within the project MINGLE (Multiresolution in Geometric Modelling), contract no. HPRN-CT-1999-00117.

## References

- [1] J. Behrens, An adaptive semi-Lagrangian advection scheme and its parallelization, *Mon. Wea. Rev.* **124**, 1996, 2386–2395.
- [2] J. Behrens, Atmospheric and ocean modeling with an adaptive finite element solver for the shallow-water equations, *Applied Numerical Mathematics* **26**, 1998, 217–226.
- [3] J. Behrens, and A. Iske, Grid-free adaptive semi-Lagrangian advection using radial basis functions, to appear in *Computers and Mathematics with Applications*.

- [4] A. Bregman, A. F. J. van Velthoven, F. G. Wienhold, H. Fischer, T. Zenker, A. Waibel, A. Frenzel, F. Arnold, F., G. W. Harris, M. J. A. Bolder, and J. Lelieveld, Aircraft measurements of  $O_3$ ,  $HNO_3$ , and  $N_2O$  in the winter arctic lower stratosphere during the stratosphere-troposphere experiment by aircraft measurements (STREAM) 1. *J. Geophys. Res.*, **100**, 1995, 11,245–11,260.
- [5] M. D. Buhmann, Radial basis functions, *Acta Numerica*, 2000, 1–38.
- [6] K. Dethloff, A. Rinke, R. Lehmann, J. H. Christensen, M. Botzet, and B. Machenhauer, Regional climate model of the arctic atmosphere. *J. Geophys. Res.*, **101**, 1996, 23,401–23,422.
- [7] N. Dyn, Interpolation and Approximation by Radial and Related Functions, in *Approximation Theory VI, Vol. 1*, C. K. Chui, L. L. Schumaker, J. D. Ward (eds.), Academic Press, 1989, 211–234.
- [8] M. Falcone, and R. Ferretti, Convergence Analysis for a Class of High-Order Semi-Lagrangian Advection Schemes, in *SIAM J. Numer. Anal.* **35:3**, 1998, 909–940.
- [9] T. Gutzmer, and A. Iske, Detection of Discontinuities in Scattered Data Approximation, in *Numerical Algorithms* **16:2**, 1997, 155–170.
- [10] K. W. Morton, *Numerical Solution of Convection-Diffusion Problems*, Chapman & Hall, London, 1996.
- [11] St. Pöhn, Implementierung eines gitterfreien adaptiven Advektions-schemas, Diplomarbeit, Technische Universität München, März 2001.
- [12] M. J. D. Powell, The theory of radial basis function approximation in 1990, in *Advances in Numerical Analysis II: Wavelets, Subdivision, and Radial Basis Functions*, W. A. Light (ed.), Clarendon Press, Oxford, 1992, 105–210.
- [13] F. P. Preparata, and M. I. Shamos, *Computational Geometry*, Springer, New York, 1985.
- [14] R. Schaback, Multivariate interpolation and approximation by translates of a basis function, in *Approximation Theory VIII*, C. K. Chui and L. L. Schumaker (eds.), World Scientific, Singapore, 1995, 491–514.
- [15] A. Staniforth, and J. Côté, Semi-Lagrangian Integration Schemes for Atmospheric Models – A Review, in *Monthly Weather Review* **119**, 1991, 2206–2223.

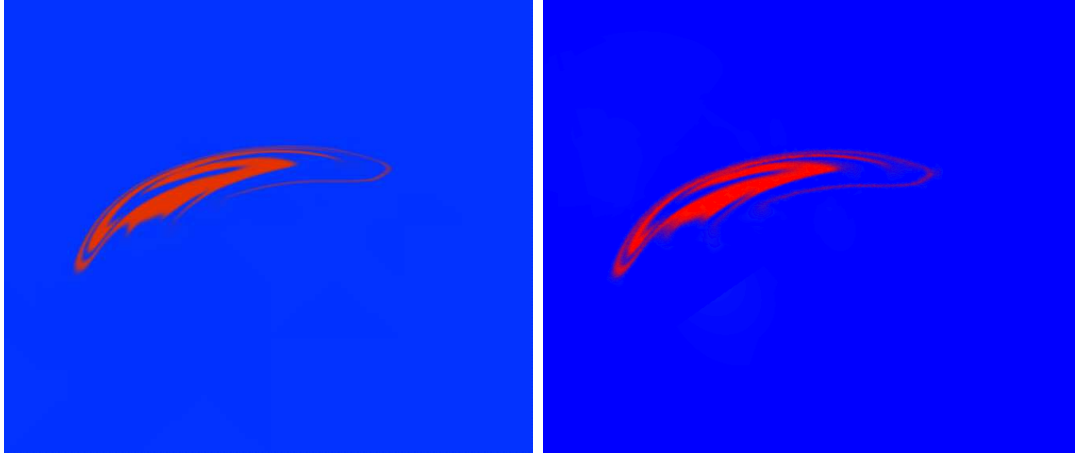


Figure 4: Results from a grid-based (left) and the grid-free (right) method for the stratospheric transport problem. The snapshots show the situation after 15 days of model time. Fine filaments can be observed in both simulations.

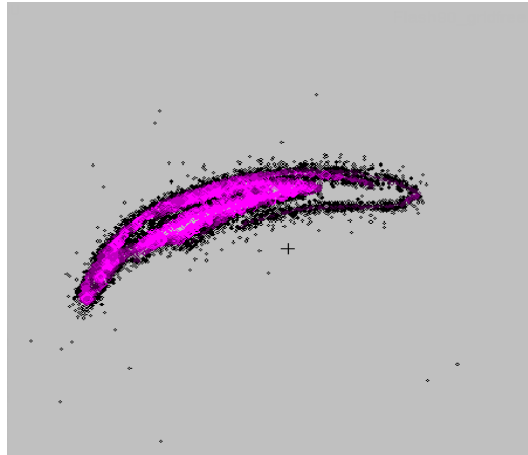


Figure 5: Node distribution of the grid-free method after 15 days. Pink colour indicates nodes with tracer concentration above 0.2.